Investigation of open channel flow with unsubmerged rigid vegetation by the lattice Boltzmann method*

He-fang JING[1,2†], Yin-juan CAI[2], Wei-hong WANG[2],
Ya-kun GUO[3‡], Chun-guang LI[2§] and Yu-chuan BAI[1]
1. State Key Laboratory of Hydraulic Engineering Simulation and Safety, Tianjin University, Tianjin 300350, China;
2. Research Institute of Numerical Computation and Engineering Applications, North Minzu University, Yinchuan 750021, China.
3. Faculty of Engineering & Informatics, University of Bradford, Bradford, BD7 1DP, UK.

Abstract: Aquatic vegetation can significantly affect flow structure, sediment transport, bed scour and water quality in rivers, lakes, reservoirs and open channels. In this study, the lattice Boltzmann method is applied for performing the two dimensional numerical simulation of the flow structure in a flume with rigid vegetation. A multi-relaxation time model is applied to improve the stability of the numerical scheme for flow with high Reynolds number. The vegetation induced drag force is added in lattice Boltzmann equation model with the algorithm of multi-relaxation time in order to improve the simulation accuracy,. Numerical simulations are performed for a wide range of flow and vegetation conditions and are validated by comparing with the laboratory experiments. Analysis of the simulated and experimentally measured flow field shows that the numerical simulation can satisfactorily reproduce the laboratory experiments, indicating that the proposed lattice Boltzmann model has high accuracy for simulating flow-vegetation interaction in open channel.

Key Words: Lattice Boltzmann method; multi-relaxation time model; aquatic vegetation; drag force; open channel flow

1. Introduction

Aquatic vegetation is one of the important components in water flow system in natural rivers,

* Project supported by the Funds for National Natural Science Foundation of China (grant number: 11861003 and 11761005).
† **Biogaraphy:** He-fang JING (1970--), male, Ph.D., Professor. **Email:** jinghef@163.com. **Tel:** +86 951 2068010 (O), +86 13259510918(M) **Address:** Research Institute of Numerical Computation and Engineering Applications, North Minzu University, Yinchuan 750021, China.
‡ Corresponding author, Email: y.guo16@bradford.ac.uk
§ Correspond author, Email: cglizd@hotmail.com

lakes, reservoirs and open channels. Aquatic vegetation can significantly affect not only the flow structure, but also the sediment transport, bed deformation, navigation, stability of banks and flood control equipment [1,2]. Due to the practical environmental and engineering importance, extensive studies have been carried out to investigate the flow-vegetation interaction and its effect on flow system by using the laboratory experiments, numerical simulation and occasionally the field observations [3-7]. In general, comparing with the numerical simulation and laboratory experiments, it is more difficult to conduct field measurement due to the limitation of appropriate instrumentations, field conditions and large cost. In past decades, laboratory experiment is one of the main tools to investigate the flow-vegetation interaction. Nepf [3] provided excellent results on flow structures of flow through emergent vegetation. The drag force induced by vegetation was investigated. Carollo *et al* [4] measured the local flow velocities for different vegetation densities, flow discharges, and flume bed slopes using two-dimensional (2D) acoustic Doppler velocimeter (ADV). Based on their experiment measurements and the Π-theorem analysis, Carollo *et al* [5] proposed an equation to estimate the flow resistance in vegetated open channel. Liu et al. [6] and Shan et al. [7] analyzed the flow direction along meandering compound channel. Wilson *et al* [8] investigated the flow structure in open channel flow for various submerged flexible vegetation. Järvelä [9] investigated the impact of the submerged flexible vegetation on the flow structure and flow resistance using flume experiment. Folkard [10] conducted laboratory experiment to investigate the flow within gaps in canopies of flexible, submerged aquatic vegetation. Ricardo *et al* [11] calculated the time and space averaged flow variables in a flume with non-uniform emergent vegetation from instantaneous velocity maps measured by using the particle image velocimeter (PIV). Liu *et al.*[12] investigated the flow features in meandering compound channel with grass on the floodplain. The effect of vegetation on sediment transport and deposition was examined by Liu and Nepf [12]. More laboratory experimental studies of flow vegetation interaction can be found in the recent excellent review of Nepf [14,15].

With the rapid development of computer technology and computational fluid dynamics techniques, various numerical models have been developed to simulate the flow characteristics in rivers and open channels. Wilson *et al* [16] studied the hydraulic impact of willow stands on the velocity distribution using a three-dimensional (3D) standard k-ε turbulence model. Guo *et al* [17] investigated the effect of the bed roughness on the flow structure in open channel using a 2D numerical model. Jing *et al* [18,19,20] applied a 2D flow turbulence model to investigate the characteristics of the water flow in meandering compound channels. Coupled with the sediment transport model, they simulated the hydrodynamics and sediment transport in the upper meandering reach of the Yellow River [21]. Huai et al. [22] applied layer approach to simulate the flow velocity field in vegetated open channel flows by considering the effect of bed roughness. Huai *et al* [23] presented results from large eddy simulation (LES) of open channel flows with non-submerged vegetation. The effect of turbulent structure on the momentum transfer across the outer line of emergent vegetation patch is evaluated by Huai *et al* [24]. Marsooli and Wu[25] examined the wave attenuation by vegetation using a 3D Reynolds-averaged Navier–Stokes equations (RANS) model. Kim *et al* [26] computed the flow and bed morphdynamics through rigid, emergent cylinders by employing a 3D LES approach.

Though these studies have demonstrated many flow features in a vegetated open channel or river flow, the complicated boundary condition of flow in vegetated rivers or open channels still poses challenges and makes it difficult for accurate simulation on the macro level. The lattice Boltzmann method (LBM), a mesoscopic method has great advantage to treat complex boundary condition and is suitable for describing the internal interactions among fluid particles and those between the fluid and external environment [27,28]. As a result, LBM has been used to simulate various complicated flow phenomenon, such as multiphase flows, flows in porous media, quasi Newtonian fluid and chemical reaction flow [29-31].

In recent years, LBM has been applied to simulate open channel flow with vegetation. Jimenez-Hornero et al developed a two-dimensional lattice model to describe the influence of vegetation on the turbulent flow structure in an open channe[32]. Yang et al developed a two-dimensional lattice Boltzmann model with a D2Q9 lattice arrangement to simulate the flow-vegetation interactions in an open channel [33]. Buxon studied the fluid dynamics of acid mine drainage flow using a lattice Boltzmann model with a D2Q9 lattice arrangement[34].

In this study, the LBM is applied to simulate the flow structure in a laboratory flume with rigid vegetation for a range of flow conditions and vegetation arrangements. The multi-relaxation time lattice Boltzmann equation (MRT-LBE) model is proposed with the specific numerical algorithm to treat the instability of the single-relaxation time (SRT) model for flows with large Reynolds number. To improve the simulation accuracy, the drag force induced by vegetation is considered in the model to take into account of the effect of vegetation on the flow field. Accompanied laboratory experiments have been carried out in a flume with vegetation to validate the numerical simulation. Three-dimensional laser Doppler velocimeter (3D LDV) is used to measure the flow velocity field.

2. Mathematical model and numerical algorithm

The Boltzmann equation that describes the spatial and temporal distribution of particle velocities is a very complex integral differential equation, which is difficult to obtain its analytic solutions [35,36] and has to be solved numerically. The LBM is the spatial, temporal, and velocity space discretized formation for Boltzmann equation, and consists of three components: the evolution equation of distribution function, the discrete velocity model and the equilibrium distribution function. In addition, the boundary conditions have to be specified to solve the equations.

2.1 The evolution equation of distribution function

The evolution equation of particle distribution function is the lattice Boltzmann equation (LBE) and can be written as [36]:

$$f_i(\mathbf{x}+\mathbf{c_i}\Delta t, t+\Delta t) = f_i(\mathbf{x},t) + \Omega_i(f), i = 0,1,2,\cdots,b-1 \tag{1}$$

where $f_i(\mathbf{x},t)$ =the ith particle distribution function, b = the number of discrete velocities, $\mathbf{c_i}$ = the ith particle velocity, Δt =the time step, $\Omega_i(f)$=the collision operator, which reflects the variation of the distribution function caused by collision.

It is difficult to solve the LBE due to the complexity of the collision term. To overcome this difficulty, Bhatnagar, Gross, and Krook simplified the equation and proposed the following lattice BGK equation (LBGK) [37,38]:

$$f_i(\mathbf{x}+\mathbf{c_i}\Delta t, t+\Delta t) = f_i(\mathbf{x},t) - \frac{1}{\tau}\left(f_i(\mathbf{x},t) - f_i^{eq}(\mathbf{x},t)\right) \tag{2}$$

where τ = the relaxation time, and $f_i^{eq}(\mathbf{x},t)$ = the local equilibrium distribution function. In SRT model, the following equilibrium distribution function is adopted[39]:

$$f_i^{eq}(\mathbf{x},t) = w_i \rho [1 + \frac{\mathbf{c_i} \cdot \mathbf{u}}{c_s^{\ 2}} + \frac{(\mathbf{c_i} \cdot \mathbf{u})^2}{2c_s^{\ 4}} - \frac{\mathbf{u} \cdot \mathbf{u}}{2c_s^{\ 2}}] \qquad (3)$$

where w_i = weight coefficient, ρ =the fluid density, $\boldsymbol{u}$ = the macro fluid velocity, c_s =the grid sound speed.

The discrete velocity model

Among the LBGK models，the widely used one is *DnQb* models developed by Qian, *et al.* [39], where *n* is the space dimension, and *b* is the number of discrete velocities. In this study, D2Q9 model is used, where the discrete velocity vectors are organized as following matrix:

$$\mathbf{c} = [c_0, c_1, \cdots, c_8] = c \begin{bmatrix} 0 & 1 & 0 & -1 & 0 & 1 & -1 & -1 & 1 \\ 0 & 0 & 1 & 0 & -1 & 1 & 1 & -1 & -1 \end{bmatrix} \qquad (4)$$

in which $c = \Delta x / \Delta t$， Δx =the spatial step.

In the model, the grid sound speed and the weight factors for corresponding distribution functions are taken as follows:

$$c_s = \frac{c}{\sqrt{3}}，\ w_0 = \frac{4}{9}，\ w_{1-4} = \frac{1}{9}，\ w_{5-8} = \frac{1}{36}.$$

The discrete velocities and their weight factors in the D2Q9 model are shown in Fig.1.

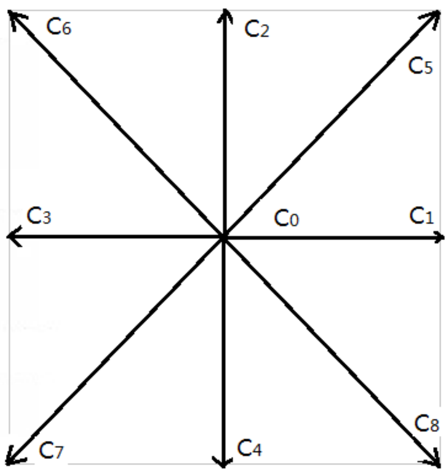

Fig. 1. The discrete velocities and their weight factors in the D2Q9 model

2.2 The MRT-LBE model

In the LBGK model, the collision operator is linearized and the computational process of LBE has been simplified. However, the application of the LBGK model is limited because of only single relaxation time is used. d'Humeriers proposed a generalized LBE (GLBE) model, which is named as multiple-relaxation-time lattice Boltzmann equation (MRT-LBE) model [35,40]:

$$f_i(\mathbf{x}+\mathbf{c_i}\Delta t, t+\Delta t) - f_i(\mathbf{x},t) = -\sum_{j=0}^{b-1}\Lambda_{ij}[f_j(\mathbf{x},t) - f_j^{eq}(\mathbf{x},t)], \quad i = 0,1,\cdots,b-1 \qquad (5)$$

where Λ_{ij} is the element of matrix Λ, and $-\Lambda = \lfloor -\Lambda_{ij} \rfloor_{b\times b}$ is named as collision matrix.

The collision step of the MRT-LBE in the velocity space is difficult to perform, and needs to be transformed. Let S be a diagonal matrix and the relationship between S and Λ be as following:

$$\mathbf{S} = \mathbf{M\Lambda M}^{-1} = diag(s_0, s_1, \cdots, s_{b-1}), \qquad (6)$$

in which **M** is called the transformation matrix. Equation (5) can then be rewritten in vector form as following:

$$\mathbf{f}(\mathbf{x}+\mathbf{c}_i\Delta t, t+\Delta t) - \mathbf{f}(\mathbf{x},t) = -\mathbf{\Lambda}[\mathbf{f}(\mathbf{x},t) - \mathbf{f}^{eq}(\mathbf{x},t)] \qquad (7)$$

where $\mathbf{f} = (f_0(x,t), f_1(x,t), \cdots, f_{b-1}(x,t))^T$.

Define **p** as:

$$\mathbf{p} = \mathbf{Mf} = [p_0, p_1, \cdots, p_{b-1}]^T, \qquad (8)$$

The following equation can be obtained by pre-multiplying matrix **M** to the both sides of (7):

$$\mathbf{p}(\mathbf{x}+\mathbf{c}_i\Delta t, t+\Delta t) - \mathbf{p}(\mathbf{x},t) = -\mathbf{S}[\mathbf{p}(\mathbf{x},t) - \mathbf{p}^{eq}(\mathbf{x},t)] \qquad (9)$$

Therefore, the component-wise of (9) can be written as:

$$p_i(\mathbf{x}+\mathbf{c_i}\Delta t, t+\Delta t) - p_i(\mathbf{x},t) = -s_i[p_i(\mathbf{x},t) - p_i^{eq}(\mathbf{x},t)], \quad i = 0,1,\cdots,b-1 \qquad (10)$$

As such, **p** can be calculated with the similar steps of the LBGK model, and **f** can then be calculated by the following transformation:

$$\mathbf{f} = \mathbf{M}^{-1}\mathbf{p} \qquad (11)$$

For the convenience of numerical simulation, pre-multiplying (9) with $\mathbf{M}^{-1}$ yields:

$$\mathbf{f}(\mathbf{x}+\mathbf{c}\Delta t, t+\Delta t) - \mathbf{f}(\mathbf{x},t) = -\mathbf{M}^{-1}\mathbf{S}[\mathbf{p}(\mathbf{x},t) - \mathbf{p}^{eq}(\mathbf{x},t)] \qquad (12)$$

The above equation can be divided into the collision step and the migration step. The collision step can be calculated as:

$$\tilde{\mathbf{f}}(\mathbf{x},t) = \mathbf{f}(\mathbf{x},t) - \mathbf{M}^{-1}\mathbf{S}[\mathbf{p}(\mathbf{x},t) - \mathbf{p}^{eq}(\mathbf{x},t)] \qquad (13)$$

where $\tilde{\mathbf{f}}(\mathbf{x},t)$ is distribution functions immediately after the collision, and the migration step is:

$$\mathbf{f}(\mathbf{x}+\mathbf{c}\Delta t, t+\Delta t) = \tilde{\mathbf{f}}(\mathbf{x},t) \qquad (14)$$

In the MRT-LBE model, the transformation matrix and the diagonal matrix for D2Q9 are[38]:

$$\mathbf{M}=\begin{pmatrix} 1 & 1 & 1 & 1 & 1 & 1 & 1 & 1 & 1 \\ -4 & -1 & -1 & -1 & -1 & 2 & 2 & 2 & 2 \\ 4 & -2 & -2 & -2 & -2 & 1 & 1 & 1 & 1 \\ 0 & 1 & 0 & -1 & 0 & 1 & -1 & -1 & 1 \\ 0 & -2 & 0 & 2 & 0 & 1 & -1 & -1 & 1 \\ 0 & 0 & 1 & 0 & -1 & 1 & 1 & -1 & -1 \\ 0 & 0 & -2 & 0 & 2 & 1 & 1 & -1 & -1 \\ 0 & 1 & -1 & 1 & -1 & 0 & 0 & 0 & 0 \\ 0 & 0 & 0 & 0 & 0 & 1 & -1 & 1 & -1 \end{pmatrix} \quad (15)$$

and

$$\mathbf{S}=diag(1,1.4,1.4,1.0,1.2,1.0,1.2,2/(1+6\nu),2/(1+6\nu))^T \quad (16)$$

where ν =fluid viscosity, and the vector **p** is defined as:

$$\mathbf{p}=(\rho,e,\varepsilon,j_x,q_x,j_y,q_y,p_{xx},p_{xy})^T \quad (17)$$

The equilibrium state vector of **p** is:

$$\mathbf{p}^{eq}=(\rho,-2\rho+3(j_x{}^2+j_y{}^2),\rho-3(j_x{}^2+j_y{}^2)^2,j_x,-j_x,j_y,-j_y,j_x^2-j_y^2,j_xj_y)^T \quad (18)$$

in which

$$j_x=\rho u_x=\sum_i f_i\, c_{ix}-F_x\Delta t,\quad j_y=\rho u_y=\sum_i f_i\, c_{iy}-F_y\Delta t\,. \quad (19)$$

where $\mathbf{F}=(F_x,F_y)^T$ = the external force.

2.3 The drag force of vegetation

Drag force induced by aquatic vegetation has great impact to water flow. Therefore, it is important to consider the aquatic vegetation induced drag force in the mathematical model. In this study, vegetation-induced drag force is considered in the MRT-LBE model, and based on the research result in [41-43], the drag force of the vegetation in the two dimensional MRT-LBE model (D2Q9) can be estimated as:

$$\mathbf{F_D}=\left(\frac{1}{2}\rho m\beta C_D DUu_x,\frac{1}{2}\rho m\beta C_D DUu_y\right) \quad (20)$$

where m =the vegetation numbers per unit area; ρ = water density; β = the constant related to the vegetation type, C_D = the drag force coefficient, D = the vegetation diameter,

$U=\sqrt{u_x{}^2+u_y{}^2}$. β = 1 when the vegetation is regular, and C_D = 1 when the Reynolds number of the vegetation ranges from 1000 to 10000.

Following three methods are usually adopted in the LBGK model to consider the effect of external force [35]: the pressure correction in the equilibrium distribution function, the velocity correction in the equilibrium distribution, and the extra force term in the evolution equation. Among these methods, the second method is relatively easy to implement to and easy to generalize in the MRT-LBE model, in which the drag forces are included. Therefore, j_x and j_y in the equilibrium distribution function in (18) are calculated as following:

$$j_x=\rho u_x=\sum_i f_i\, c_{ix}-\frac{1}{2}\rho m\beta C_D DUu_x,\qquad j_y=\rho u_y=\sum_i f_i\, c_{iy}-\frac{1}{2}\rho m\beta C_D DUu_y \tag{21}$$

2.4 Boundary conditions

The laboratory flume is symmetric about the center line of the flume, and the vegetation group is symmetric about the center line. Therefore, in order to save the simulation time, only the flow region from the left wall to the center line of the flume is simulated in the numerical computation. As a result, the symmetric boundary condition is adopted at the center line, as shown in Fig. 2.

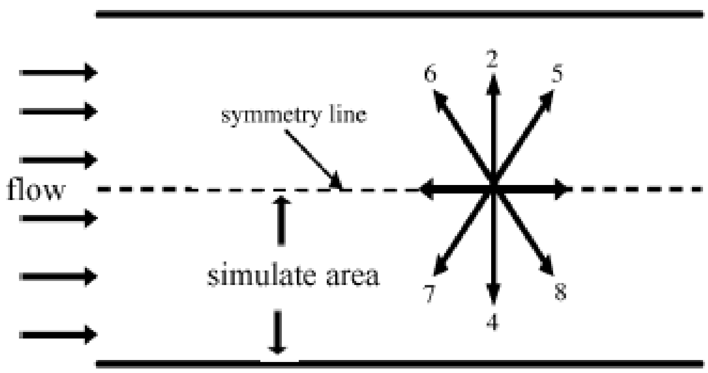

Fig. 2. The symmetry boundary condition of D2Q9

If the simulated area is from the south wall to the center line, then the unknown distribution functions (f_4, f_7 and f_8) at the center line can be calculated as follows:

$$f_4=f_2,\ f_8=f_5,\ f_7=f_6. \tag{22}$$

At the inlet boundary (west), the flow velocity is known, and the following conditions can be derived [38]:

$$\rho_w = \frac{1}{1-u_w}(f_0 + f_2 + f_4 + 2(f_3 + f_6 + f_7)), \qquad (23)$$

$$f_1 = f_3 + \frac{2}{3}\rho_w u_w, \qquad (24)$$

$$f_5 = f_7 - \frac{1}{2}(f_2 - f_4) + \frac{1}{6}\rho_w u_w + \frac{1}{2}\rho_w v_w, \qquad (25)$$

$$f_8 = f_6 + \frac{1}{2}(f_2 - f_4) + \frac{1}{6}\rho_w u_w - \frac{1}{2}\rho_w v_w. \qquad (26)$$

where u_w = the velocity at the inlet, and it is given in a parabolic distribution along the cross-section:

$$u_w = 4u_{\max}\left(\frac{y}{B} - \frac{y^2}{B^2}\right) \qquad (27)$$

In which, $u_{\max}$ = the maximum velocity at the inlet; B = the width of the channel; y = the transverse distance from the left bank of the channel.

At the outlet boundary (east), the following full development boundary condition is used：

$$f_{k,n} = f_{k,n-1}, k = 0,...,8. \qquad (28)$$

At the solid wall boundary (south boundaries and the vegetation), the bounce back boundary condition is applied [36], as shown in Fig. 3. For example, at the south wall, the unknown distribution functions f_5, f_2, f_6 can be obtained as $f_5 = f_7, f_2 = f_4, f_6 = f_8$, in which f_7, f_4, f_8 at the node (1,1) can be calculated by migrating the neighbor nodes, i.e. $f_7(i,1) = f_7(i+1,2)$, $f_4(i,1) = f_4(i,2)$, $f_8(i,1) = f_8(i-1,2)$.

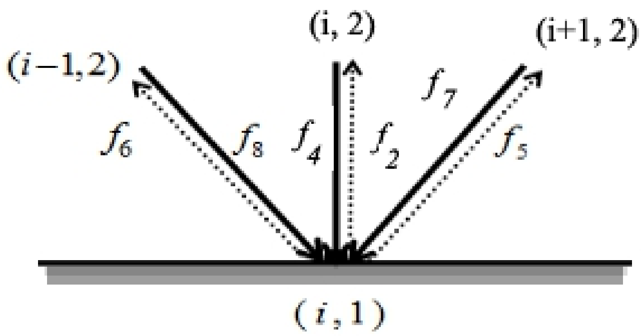

Fig. 3. The bound back condition at south wall

2.5 The algorithm of MRT-LBE with drag force induced by vegetation

It is important to design an algorithm of the MRT-LBE model that can consider the influence of the vegetation-induced drag force on the flow structure in order to improve the accuracy of the numerical simulation. The algorithm of the MRT-LBE model with drag force induced by vegetation can be described as follows.

Step 1. Mesh generation

As the computational domain is rectangular, the square grids are used to divide the domain and the spatial and computational time steps are set as unit (=1).

Step 2. Initial conditions

The initial velocities, density and distribution functions are specified as following:

Velocities at x and y directions (u_x and u_y) are set as zero at all grids except for inlet grids; the initial density ($\rho = 1$) is set as 1; the initial distribution function is set as $f_i = w_i \rho, i = 0,1,\ldots,b-1$, where w_i is the weighting factor along the i-th direction.

Step 3.Calculation of $\mathbf{p}^{\mathbf{eq}}(\mathbf{x},t)$ and $\mathbf{p}(\mathbf{x},t)$

$\mathbf{p}^{\mathbf{eq}}(\mathbf{x},t)$ can be calculated according to (18) and $\mathbf{p}(\mathbf{x},t)$ is obtained from (8).

Step 4. Collision step

The distribution function after collision ($\tilde{\mathbf{f}}(\mathbf{x},t)$) is calculated by (13).

Step 5. Migration step

The distribution function of the next time step ($\mathbf{f}(\mathbf{x}+\mathbf{c}\Delta t, t+\Delta t)$) is calculated by (14).

Step 6. Boundary conditions

At the inlet, u_w and v_w are specified, ρ_w and unknown distribution functions are calculated by (23)-(26). At the outlet, full development boundary condition is used, and the unknown distribution functions can be calculated by (28). At the solid wall (solid boundary of the flume and the vegetation), bounce back boundary condition is applied. At the center line of the flume, the symmetry boundary condition is adopted and the unknown distribution functions can be get by (22).

Step 7. Calculation of macroscopic physical quantities

The macroscopic physical quantities can be calculated as follows after distribution functions have been obtained:

$$\rho = \sum_{i=0}^{b-1} f_i \ , \quad u_x = \frac{1}{\rho} \sum_{i=0}^{b-1} f_i \, c_{ix} \, , \quad u_y = \frac{1}{\rho} \sum_{i=0}^{b-1} f_i \, c_{iy} \tag{29}$$

Steps 3 - 7 are repeated until a prescribed time step is reached.

3. Description of experiment and numerical simulation

3.1 Description of laboratory experiment

In order to validate the numerically simulated results, physical laboratory experiments have been carried out using a flume, which is 15m length, 0.49m width and 0.5m depth. The 3D LDV is used to measure the flow velocity field. Glass rods with three diameters of *D*=10mm, 8mm and 6mm and the height of 0.5m are used to simulate unsubmerged vegetation in experiments. Because the flow characteristics of vegetation with different diameters is similar, only the measured results with rod diameter of 10mm are presented and discussed in this paper.

Four typical cases are chosen for experiments with different vegetation arrangements, as listed in Table 1 in which the flow Reynolds number and the vegetation Reynolds number are calculated as follows:

$$\mathrm{Re}_w = U_{in} R_{in} / \nu \tag{30}$$

$$\mathrm{Re}_v = U_{in} D / \nu \tag{31}$$

where U_{in}, R_{in} are the averaged flow velocity and hydraulic radius at the flow inlet, respectively; ν is the water viscosity coefficient. Water flow discharge is kept as 0.054m^3/s for all the four cases.

Table 1. Basic conditions of the four typical cases

Case	Vegetation's arrangement	Water depth /m	Hydraulic radius /m	Inlet velocity /m/s	Vegetation Number	Flow Reynolds number	Vegetation Reynolds number
1	Sparse and staggered	0.206	0.112	0.529	38	59199	5296
2	Dense and staggered	0.254	0.125	0.430	149	53625	4300
3	Sparse and parallel	0.189	0.107	0.577	35	61562	5772
4	Dense and parallel	0.235	0.120	0.464	143	55656	4642

The first row of glass rods was arranged 8.48m from the inlet of the flume. The row and column numbers of the rods for dense conditions were 11 and 13, respectively; while for sparse conditions, they were 5 and 7, respectively. Both the longitudinal and transverse distances between two neighbor rods were 81.7mm for Cases 1 and 3, and were 40.8mm for Cases 2 and 4. The length of the vegetation area was 0.49 m for all the four cases. The position of the glass rods was shown in Fig. 4.

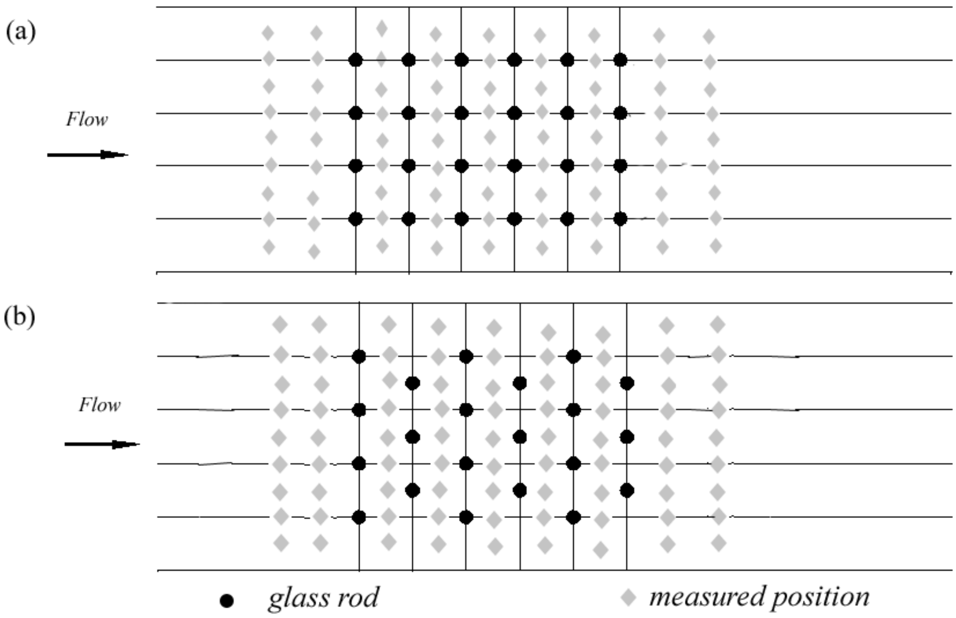

Fig. 4. Sketch of the rods and measured position

Several cross sections were chosen as the measurement sections, as shown in Fig. 4. In particular, a cross-section between two columns of rods was set as a measurement section to investigate the flow structures within the vegetation. In addition, flow structures were measured at two cross-sections upstream and downstream of the vegetation area. Along the vertical direction, measurements were taken every 10mm from the flume bed to water surface.

3.2 Description of the simulated area and mesh generation

It would be expensive and unnecessary to set the whole flume as computational domain. As one is only interested in the flow characteristics around the vegetation patch, a region of 1.53m×0.49m, covering the vegetation patch, is chosen as the computational domain. The domain is 8.48m from the inlet of the flume. The vegetation patch is 0.49m long and 0.49m wide, as shown in Fig. 5.

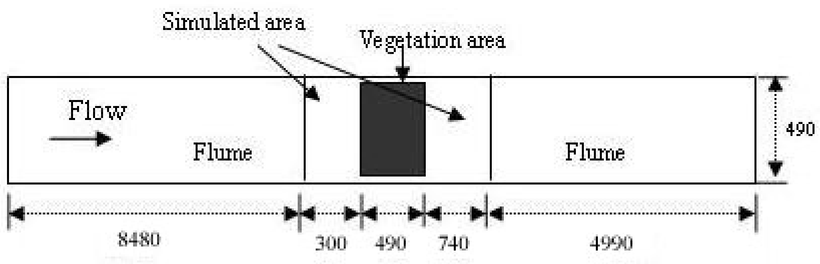

Fig. 5. Sketch of simulated area and vegetation area in the laboratory flume (unit: mm)

The simulated area is a rectangle with 1.53m long (in the x-direction) and 0.49m wide (in the y-direction). Because the flume and the flow condition are symmetry along the y-direction, only a half of the area is used for numerical simulation. So the actual simulated area is 1.53m long in the x-direction and 0.245m wide in the y-direction.

1200 grids and 192 grids are assigned along the x- and y- directions, respectively. There are 1200×192 = 230400 grid cells for the whole simulated area. Each of the glass rods are covered by 7.8 grids along both the x- and y- directions, as shown in Fig. 6.

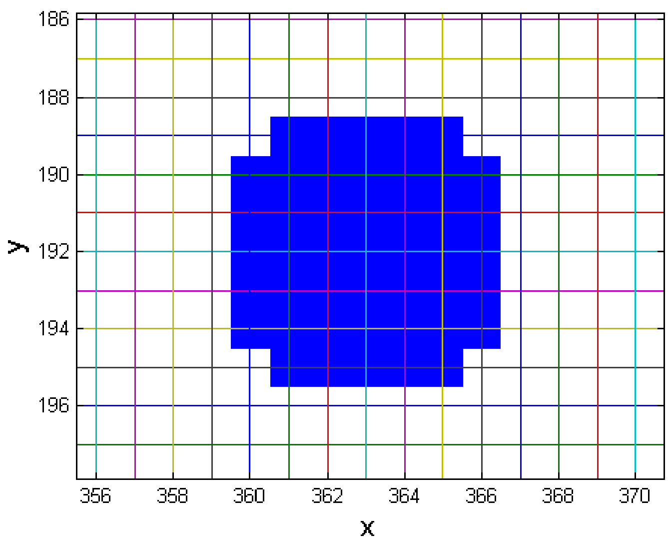

Fig. 6. The mesh around a typical glass rod

4. Results and discussion

4.1 Evaluation of numerical convergence

To investigate the convergence of the MRT-LBE numerical model, numerical tests have been carried out with three different grid resolutions for Case 1. These runs have grid numbers of

N=600×192, 1200×384 and 2400×768, respectively, these grids correspond respectively to the vegetation spacing of 40.85, 81.7 and 163.4 mm, In order to estimate the convergence, the numerical error of any run (E) is assumed to be proportional to l^n, where l is the mesh size, and n is the order of the convergence [44]. Letting E_N and l_N denote the numerical error and mesh size with grid numbers of N, respectively, then

$$E_N \approx \alpha (l_N)^n$$

Where α is a constant. It is noticed that $l_{600\times192} = 2l_{1200\times384} = 4l_{2400\times768}$, and as a result, the following formula can be obtained.

$$\frac{E_{600\times192} - E_{1200\times384}}{E_{1200\times384} - E_{2400\times768}} \approx \frac{(l_{600\times192})^n - (l_{1200\times382})^n}{(l_{1200\times384})^n - (l_{2400\times768})^n} = \frac{(2l_{1200\times384})^n - (l_{1200\times384})^n}{(l_{1200\times384})^n - (\frac{1}{2}l_{1200\times384})^n} = \frac{2^n - 1}{1 - 2^{-n}} = 2^n$$

An averaged value of the left hand side of above formula is 3.3. Therefore, the order of convergence for the numerical method is about 1.7.

4.2 Comparison between simulated and measured data

Before simulation using the LBM, it is usually to transform all the physical variables into non-dimensional form (lattice units)[38]. Let ρ_P, L_p, W_P, D_P, U_P, Re_P, ν_P, F_P and ρ_L, L_L, W_L, D_L, U_L, Re_L, ν_L, F_L be the density of water, length of the flume, width of the flume, diameter of the rods, flow velocity, Reynolds number, fluid kinematic viscosity and drag force of vegetation in the physical area and the computational domain, respectively, then these variables must satisfy the following relationships:

$$\frac{L_P}{L_L} = \frac{W_P}{W_L} = \frac{D_P}{D_L} \tag{32}$$

$$\mathrm{Re}_P = \frac{U_P D_P}{\nu_P} = \frac{U_L D_L}{\nu_L} = \mathrm{Re}_L \tag{33}$$

$$\frac{F_P}{F_L} = \frac{\rho_P}{\rho_L}\left(\frac{D_L}{D_P}\right)^2\left(\frac{\mu_P}{\nu_L}\right)^2 \tag{34}$$

Equations (32) and (33) indicate that the non-dimensional form of the basic parameters in the computational domain are calculated, as shown in Table 2. For the convenience of comparison, the dimensional basic parameters are also presented.

Table 2. Basic parameters in dimensional and non-dimensional forms

Cases	Dimensional form					Non-dimensional form				
	U_{in} /m/s	L /m	W /m	D /m	v m^2/s	U_{in}	L	W	D	v
1	0. 529	1. 53	0. 49	0. 01	1. 31E-06	0. 20	1200	384	7. 84	0. 00039
2	0. 430	1. 53	0. 49	0. 01	1. 31E-06	0. 16	1200	384	7. 84	0. 00038
3	0. 577	1. 53	0. 49	0. 01	1. 31E-06	0. 22	1200	384	7. 84	0. 00039
4	0. 464	1. 53	0. 49	0. 01	1. 31E-06	0. 18	1200	384	7. 84	0. 00040

In order to investigate the effect of vegetation on flow structure, two simulations have been performed with one considering the vegetation-induced drag force and another without considering the drag force generated by vegetation. For convenient comparison, the measured velocity is converted into non-dimension form as shown in Fig. 7.

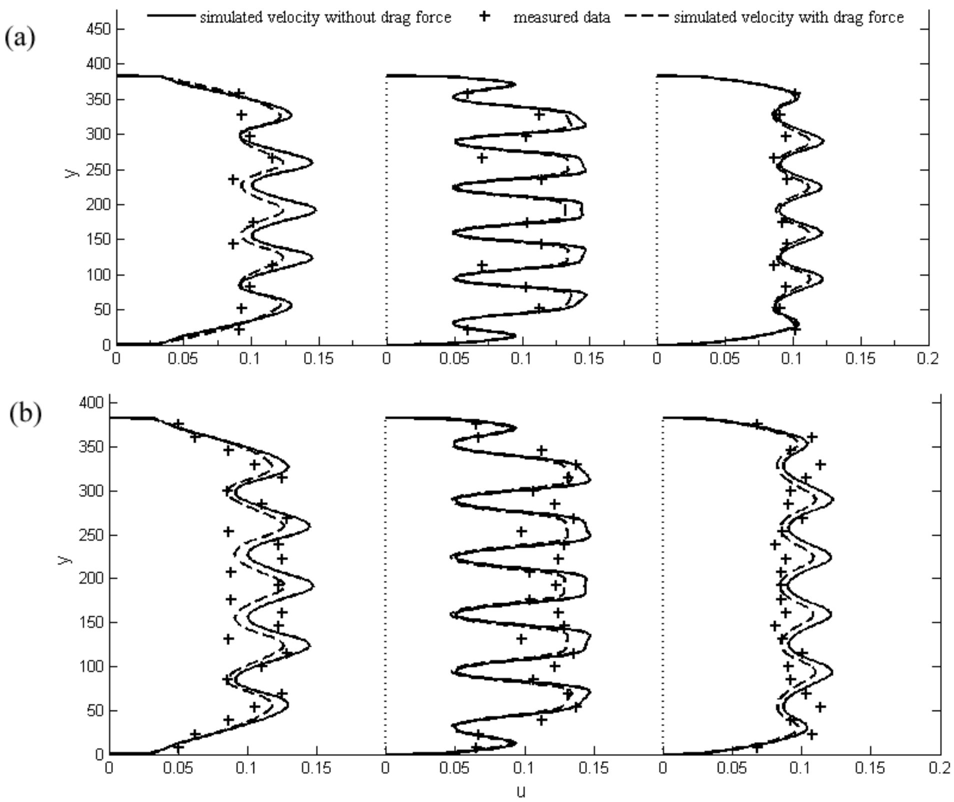

Fig. 7. Comparison between the simulated and measured velocities (a) Case 1； (b) Case 2

Three cross sections (3 lines perpendicular to the banks of the channel) at the middle of two adjacent columns of vegetation are chosen for comparison. The distances of these sections from the inlet are 347, 443 and 539, respectively.

Fig. 7 shows that the simulated flow velocity decreases when the drag force generated by vegetation is considered. It is seen that the simulated velocity with vegetation-induced drag force agrees well with the laboratory measurements, while there exists some discrepancy between the simulation and measurement when the drag force generated by vegetation is ignored in the numerical model. This indicates that the numerical simulation accuracy can be improved when the vegetation-induced drag force is taken into account.

Figure 7 also shows that the flow velocity filed is an indented distribution. The flow behind glass rods is held back due to the blockage effect caused by them. As a result, the flow velocity decreases greatly behind the rods. Meanwhile, the flow velocity between rods increases. A little difference is found between the simulated and measured velocities. In general, the simulated velocity field is in good agreement with the measured one when the vegetation-induced drag force is considered.

4.3 Comparison among numerically simulated results

Fig. 8 shows the simulated velocity distributions for Cases 1-4. It can be found that the velocity distributions largely depend on the arrangement of the rods. In the upstream of the computational domain, i.e. from the inlet to the first column of the vegetation, the flow velocity shows a parabolic distribution along the transverse direction for all the four cases. In the vegetation area, i.e. from the first column of rods to the last column of rods, the velocity distribution is very complicated. Flow velocity becomes smaller near the rods, while it is larger near the middle of two adjacent rows of rods. When the rods are staggered (Cases 1 and 2), the main stream lines are not parallel to the channel banks due to the complex blockage effect generated by staggered rods. However, when the rods are parallel, the main stream lines are approximately parallel to the channel banks. Moreover, it can be found that the velocity between two adjacent rod rows is parabolic distribution along the transverse direction.

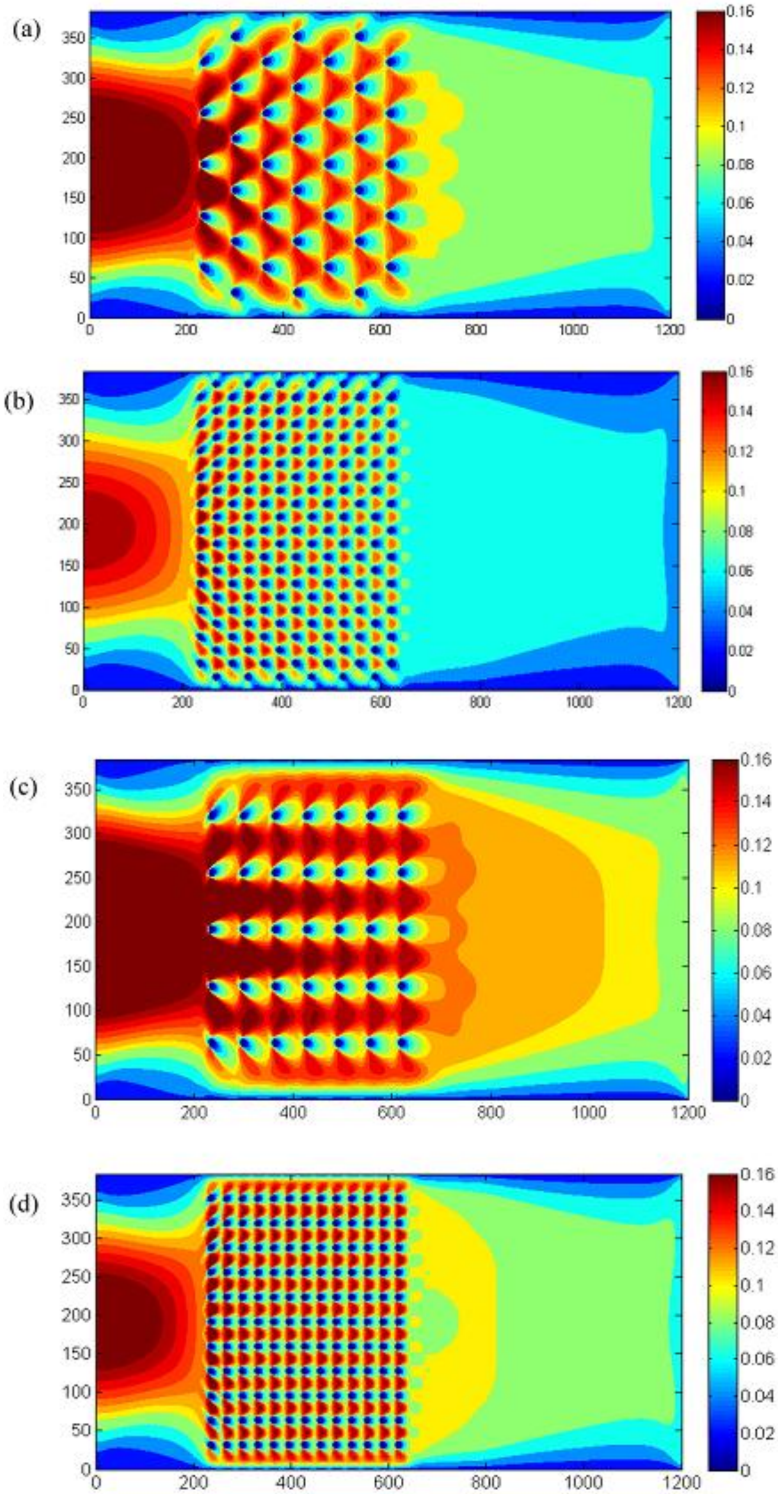

Fig. 8. Comparison of the flow velocity contour among four typical cases (a) Case 1; (b) Case 2; (c) Case 3; (d) Case 4.

In the downstream of the vegetation area, i.e. from the last column of vegetation to the outlet, when the rods are denser and staggered (Case 2), flow velocity reaches the smallest and the most uniform among the four cases. This means that such rod arrangement generates the largest blockage effect and flow resistance to water flow. Meanwhile, when the rods are sparse and parallel (Case 3), the flow velocity reaches the largest and the mostly uniform among the four cases, indicating that the smallest flow resistance is generated by such rod array.

Fig. 9 is the flow velocity field within the vegetation area for all four cases to clearly show the flow characteristics. It is seen that the flow velocity field is very complex in the vegetation area, especially when the rods are staggered (Cases 1 and 2). Secondary flow circulation is seen to form close to rod when water flow passes the rod. In order to show the flow field more clearly, the flow field around some typical rods in Case 2 is enlarged, as shown by Fig. 10.

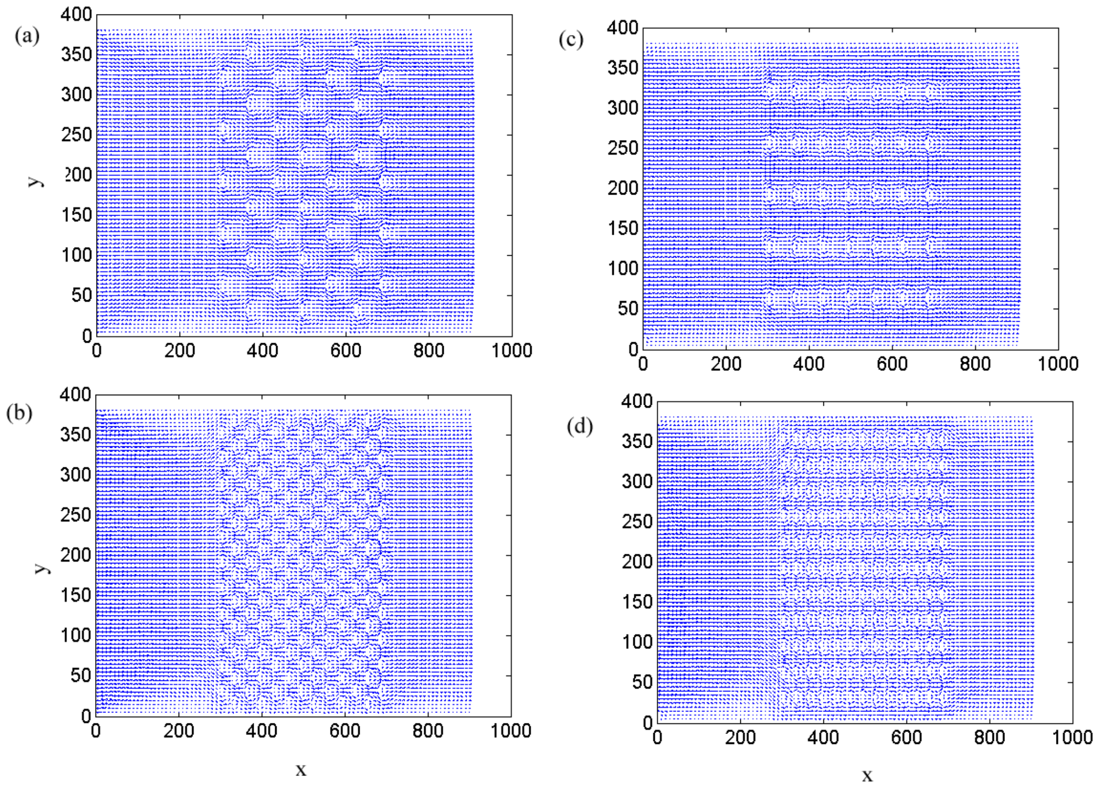

Fig. 9. Flow velocity field in the vegetation area of four cases (a) Case 1; (b) Case 2; (c) Case 3; (d) Case 4

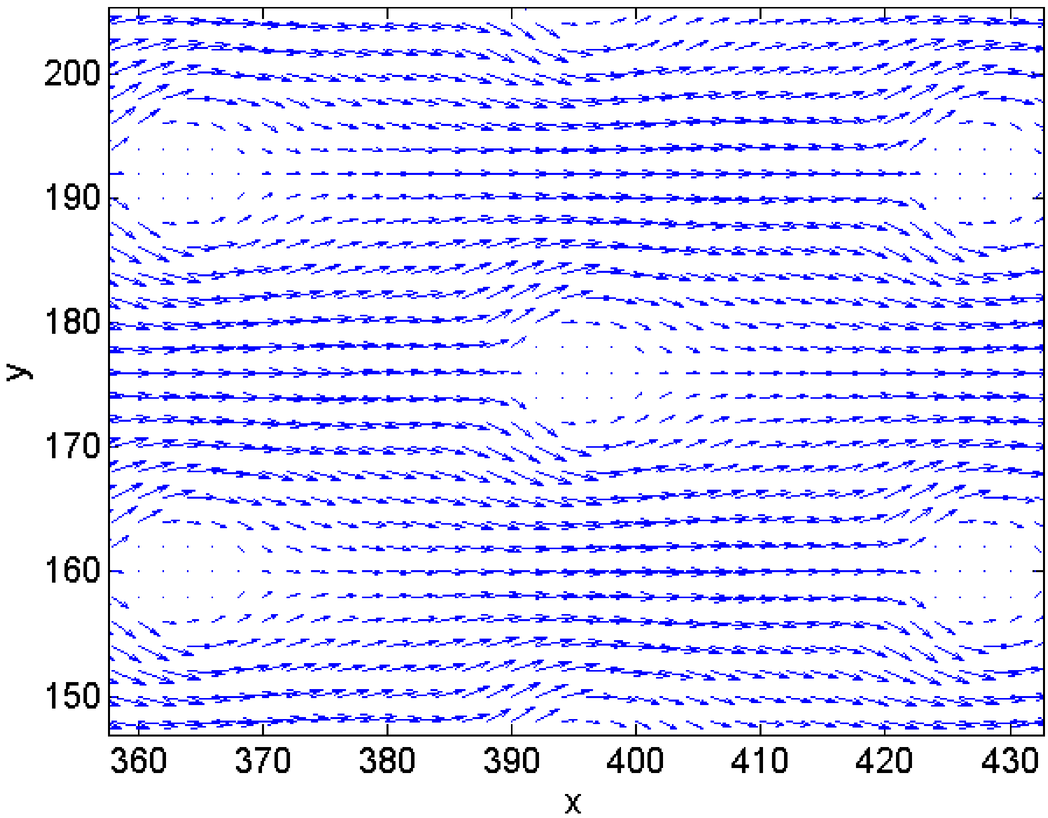

Fig. 10. Flow field around some typical rods in Case 2

Fig. 11 shows the flow streamlines for the four cases. It is seen that the oscillation of streamlines appears when flow passes through the vegetation area. Such streamline oscillation diminishes and dies out after flow exits the vegetation area. In the vegetation area, the streamlines are approximately parallel to the channel banks when the rods are parallel, while the streamlines become very complicated when the rods are staggered. In order to show the streamline more clearly, the streamline around some typical rods in Case 2 is presented, as shown in Fig. 12.

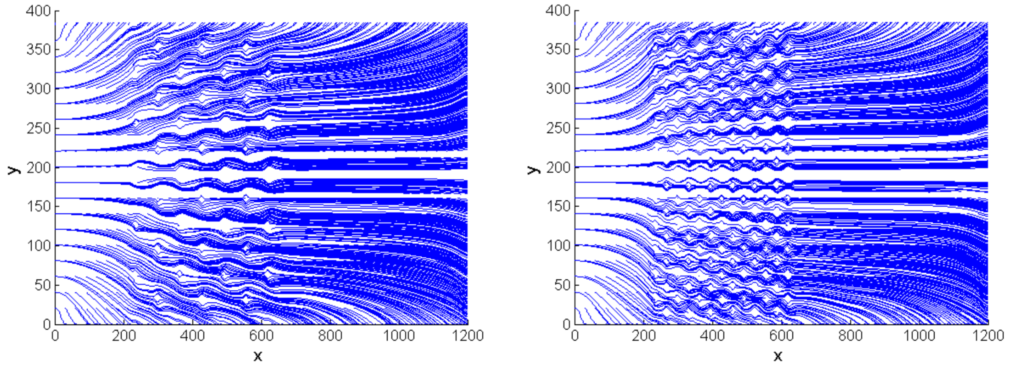

(a) Case 1 (b) Case 2

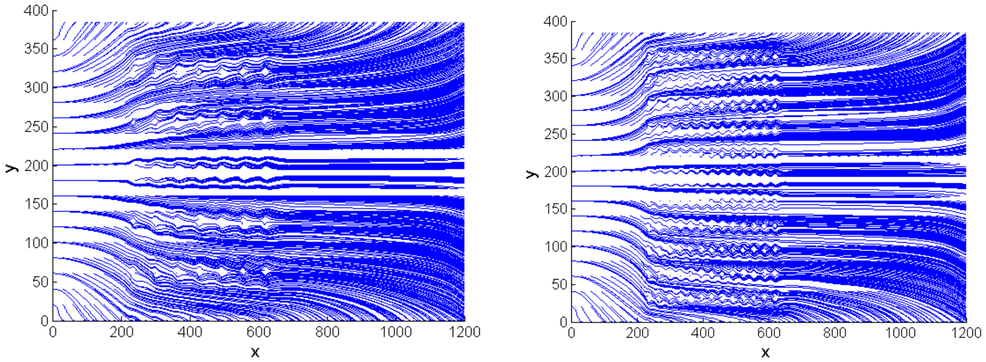

(c) Case 3 (d) Case 4

Fig. 11. Flow streamlines of four typical cases

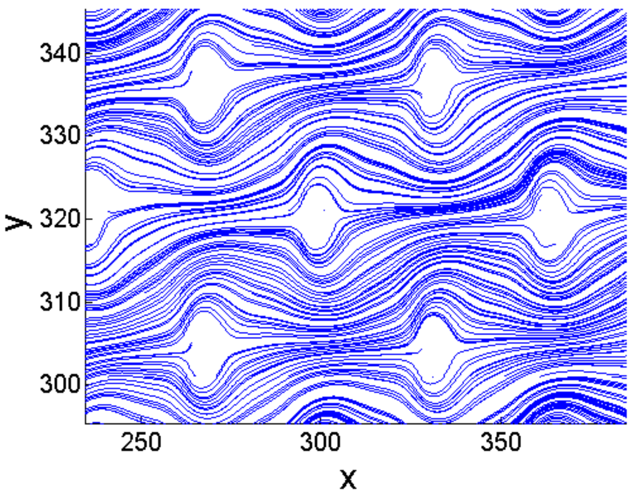

Fig. 12. Flow streamline around some typical rods in Case 2

Fig. 13 shows the flow field at five typical cross sections for Cases 1-4 to investigate the effect of different arrangements of vegetation on flow structure. Section 1 locates upstream of the simulated area (x=118); Sections 2, 3 and 4 locate at the middle of two adjacent columns of vegetation (x=347, 443 and 539, respectively); and Section 5 locates downstream of the simulated area (x=910).

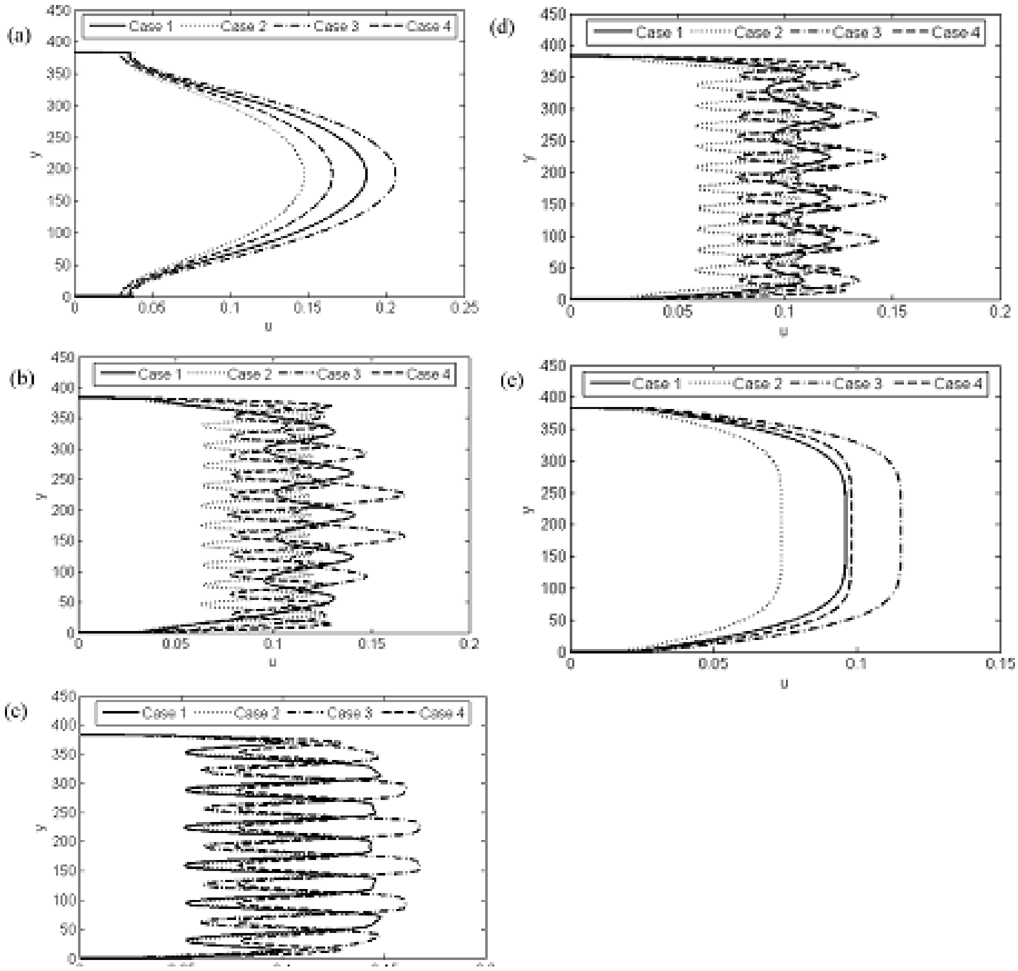

Fig. 13. Comparison of the simulated velocities among four typical cases on four typical cross-sections: (a) Section 1 (x=118); (b) Section 2 (x=347); (c) Section 3 (x=443); (d) Section 4(x=539); (e) Section 5 (x=910)

It is well known that the velocity distribution along transverse direction in a channel without vegetation is usually parabolic. However, in a channel with vegetation, the velocity distribution is quite different. Fig. 13 (a) shows that the flow velocity distribution at the upstream of the vegetation patches is parabolic. It is seen from Fig. 13(a) that the averaged velocities of Cases 1 and 3 are larger than those of Cases 2 and 4 on Section 1, indicating that the flow with sparse vegetation arrangement encounters small flow resistance than that with denser vegetation arrangement.

The velocity distributions at Sections 2-4 are indented, as shown in Fig. 13(b), (c) and (d). Right behind each glass rod, flow velocity is smaller due to the blockage effect induced by rods. However, the velocity is larger at other area because of the narrowing of the wetted cross-section area. It can also be found that the averaged velocities of Cases 1 and 3 are larger than those of Cases 2 and 4, respectively.

The flow on Section 5 is still affected by vegetation-induced drag force. As shown in Fig. 13(e), flow velocity at Section 5 is shown as a U-shape distribution for all these cases, indicating that the flow velocity is close to uniform distribution along transverse direction after the flow passes through the vegetation area. The averaged velocity increase in turn for Case 2, Case 1, Case 4 and Case 3.This means that the flow resistance is the strongest when the rods are denser and staggered, while the flow resistance reaches the weakest when the rods are sparse and parallel. The flow resistance is between the above conditions when the rods are in dense and parallel arrangement, or in sparse and staggered arrangement.

4.4 Comparison of drag force in the vegetation area

Drag force of the vegetation plays an important role in the flow field of vegetation area can be calculated by (20). Because the drag force distributions of four cases are similar, only the contour lines of drag force in Cases 1 and 3 are presented, as shown in Fig. 14. It is seen that the distribution of drag force in the vegetation area is very complicated. Generally speaking, the drag force near the upstream of vegetation area is larger than that downstream.

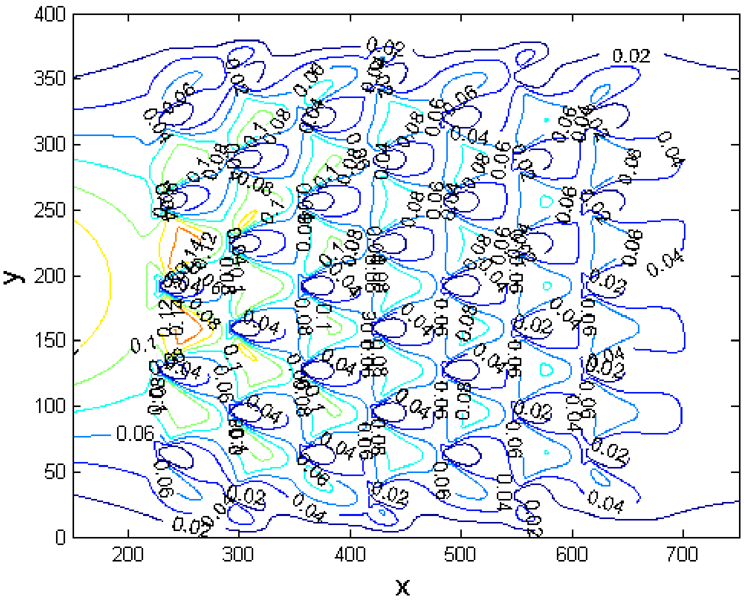

(a) Case 1

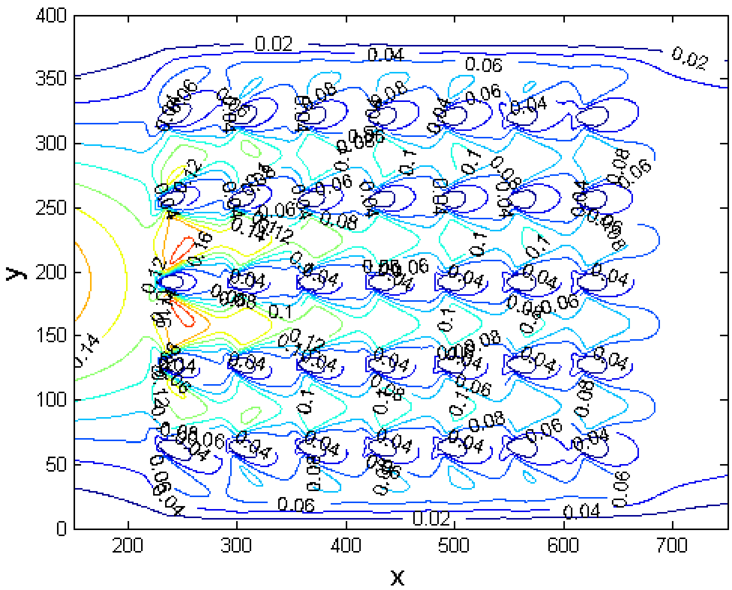

(b) Case 3

Fig. 14. The contour lines of drag force in the vegetation area (unit: N/m3)

5. Conclusion

In this study, D2Q9 model in LBM with the numerical algorithm is proposed for numerical simulation is applied for performing 2D numerical simulation of the flow in an open channel with unsubmerged rigid vegetation. The MRT-LBE model is applied to improve the stability of

LBGK model for flow with high Reynolds number. The vegetation-induced drag force is added in the MRT-LBE model to improve the simulation accuracy.

Based on the analysis of the numerical simulated results, the followings conclusions can be obtained:

(1) Good agreement between the simulated and measured velocity indicates that the MRT-LBE model is capable of simulating the water flow in open channels with various arrangements of vegetation arrays.

(2) The flow velocity distribution is parabolic at cross-sections upstream and U-shaped curve downstream of the vegetation patch in open channel, indicating that vegetation can greatly affect the flow structure downstream to some extent. However, such effect is weaker than that within the vegetation area.

(3) The flow velocity is indented distribution at the cross-sections within the vegetation area due to the vegetation-induced drag force. Generally speaking, due to the blockage effect, flow velocity behind a glass rod is relatively small, while the flow velocity between two adjacent rows is relatively large because of the contraction effect.

(4) The flow velocity within the vegetation area is larger for sparse arrangements of vegetation than for denser arrangements of vegetation. This is because that the denser vegetation will generate larger flow resistance than the sparse vegetation for otherwise identical conditions.

(5) Generally speaking, drag force near the upstream of vegetation area is larger than that generated downstream.

(6) The numerical convergence is evaluated for the MRT-LBE model. The order of the numerical convergence is found to be about 1.7.

Acknowledgments: The authors gratefully acknowledge the support of the National Natural Scientific Foundation of China (Nos. 11861003 and 11761005), the Foreign Expert Project of North Minzu University, China. The authors declared that the manuscript does not contain clinical studies or patient data. Reviewers' comments have greatly improved the quality of the paper.

References

[1] KANG H. Flow Characteristics and morphological changes in open-channel flows with alternate vegetation zones[J]. **KSCE Journal of Civil Engineering,** 2013,17(5): 1157-1165.

[2] DEVI T. B., and Kumar B. Experimentation on submerged flow over flexible vegetation patches with downward seepage [J]. **Ecological Engineering,** 2016,91: 158–168.

[3] NEPF H. M. Drag, turbulence, and diffusion in flow through emergent vegetation [J]. **Water Resources Research,** 1999,35(2), 479-489.

[4] CAROLLO F. G., FERRO V. and TERMINI D. Flow velocity measurements in vegetated Channels [J]. **ASCE Journal of Hydraulic Engineering,** 2002,128: 664-673.

[5] CAROLLO F. G., FERRO V. and TERMINI D. Flow resistance law in channels with flexible submerged vegetation [J]. **ASCE Journal of Hydraulic Engineering,** 2005,131(7): 554-564.

[6] LIU, X., ZHOU, Q., HUANG, S., et al. Estimation of flow direction in meandering compound channels. **Journal of Hydrology**, 2018. 556, 143-153.

[7] SHAN, Y.Q., HUANG, S., LIU, C., et al. Prediction of the depth-averaged two-dimensional flow direction along a meander in compound channels. **Journal of Hydrology**, 2018, 565, 318-330.

[8] WILSON C. A. M. E., STOESSER T. and BATES P. D. et al. Open channel flow through different forms of submerged flexible vegetation[J]. **ASCE Journal of Hydraulic Engineering,** 2003,129(11): 847–853.

[9] JARVELA J. Effect of submerged flexible vegetation on flow structure and resistance. **Journal of Hydrology,** 2005,307(1-4): 233-241.

[10] FOLKARD A. M. Flow regimes in gaps within stands of flexible vegetation: laboratory flume simulations [J]. **Environmental Fluid Mechanics,** 2011,11(3): 289–306.

[11] RICARDO A. M., FRANCA M. J. and FERREIRA R. M. L. Turbulent flows within random arrays of rigid and emergent cylinders with varying distribution [J]. **ASCE Journal of Hydraulic Engineering,** 2016,142(9): 1-6.

[12] LIU C., SHAN Y. Q. and LIU X. N. et al. The effect of floodplain grass on the flow characteristics of meandering compound channels[J]. **Journal of Hydrology,** 2016,542: 1-17.

[13] LIU C., NEPF H. Sediment deposition within and around a finite patch of model vegetation over a range of channel velocity. **Water Resources Research,** 2016, 52(1): 600-612.

[14] NEPF H. M. Flow and transport in regions with aquatic vegetation [J]. **Annual review of fluid mechanics,** 2012,44(1): 123-142.

[15] NEPF H. M. Hydrodynamics of vegetated channels[J]. **Journal of Hydraulic Research**, 2012,50 (3): 262-279.

[16] WILSON C. A. M. E., YAGCI O. and RAUCH H. P. et al. 3D numerical modelling of a willow vegetated river/floodplain system[J]. **Journal of Hydrology,** 2006,327(1-2): 13-21.

[17] GUO Y. K., ZHANG L. X. and SHEN Y. M. et al. Modelling study of free overfall in a rectangle channel with strip roughness [J]. **ASCE Journal of Hydraulic Engineering,** 2008,134(5): 664-668.

[18] JING H. F., GUO Y. K. and LI C. G. et al. Three dimensional numerical simulation of compound meandering open channel flow by Reynolds stress equation model [J]. **International Journal for Numerical Methods in Fluids,** 2009,59: 927-943.

[19] JING H. F. LI C., GUO, Y. K. et al. Numerical simulation of turbulent flows in trapezoidal meandering compound open channels. International Journal for Numerical Methods in Fluids, 2011, 65:1071-1083.

[20] JING H. F., LI Y. T., LI C. G. Numerical study of flow in the Yellow River with non-monotonous banks[J]. **Journal of Hydrodynamics,** 2016，28(1):142-152.

[21] JING H. F., LI C. G. and Guo Y. K. et al. Modelling of sediment transport and bed deformation in rivers with continuous bends[J]. **Journal of Hydrology,** 2013,499: 224-235.

[22] HUAI, W.X., CHEN, Z. and HAN, J, Mathematical model for the flow with submerged and emerged rigid vegetation. **Journal of Hydrodynamics**, 2009. 21(5): 722–729.

[23] HUAI W. X., WU Z. L. and QIAN Z. D. et al. Large eddy simulation of open channel flows with non-submerged vegetation [J]. **Journal of Hydrodynamics,** 2011,23(2): 258-264.

[24] HUAI W. X., XUE W. and QIAN Z. D. Large-eddy simulation of turbulent rectangular open-channel flow with an emergent rigid vegetation patch[J]. **Advances in Water Resources,** 2015,80: 30–42.

[25] MARSOOLI R., WU W. M. Numerical investigation of wave attenuation by vegetation using a 3D RANS model. **Advances in Water Resources,** 2014, 74: 245-257.

[26] KIM H. S., NABI M., KIMURA I., and SHIMIZU Y. Computational modeling of flow and morphodynamics through rigid-emergent vegetation [J]. **Advances in Water Resources,** 2015, 84: 64-86.

[27] CHEN S. Y., DOOLEN G. D. Lattice Boltzmann method for fluid flows. **Annual Review of Fluid Mechanics,** 30:329-364.

[28] MCNAMARA G. R., ZALESKI G. Use of the Boltzmann equation to simulate lattice gas automata. **Physical Review Letters,** 1998,61(20): 2332-2335.

[29] AYODELE S. G., VARNIK F. and RAABE D. Lattice Boltzmann study of pattern formation in reaction-diffusion systems[J]. **Physical Review E: Statistical, Nonlinear & Soft Matter Physics,** 2011,83(1-2): 4826-4834.

[30] HUANG R. Z., Wu H.Y. and CHENG P. A new lattice Boltzmann model for solid–liquid phase change[J]. **International Journal of Heat and Mass Transfer,** 2013, 59: 295-301.

[31]LI Q., LUO K. H. and KANG Q. J. et al. Lattice Boltzmann methods for multiphase flow and phase-change heat transfer[J]. **Progress in Energy and Combustion Science,** 2016,52: 62-105.

[32] JIMENEZ-HORNERO F. J., Girάldez J V, Laguna A M, et al. Modelling the effects of emergent vegetation on an open-channel flow using a lattice model [J]. **International Journal for Numerical Methods in Fluids**, 2010, 55(7):655-672.

[33] YANG Z., BAI F., HUAI W., et al. Modelling open-channel flow with rigid vegetation based on two-dimensional shallow water equations using the lattice Boltzmann method [J]. **Ecological Engineering**, 2017, 106:75-81.

[34] BUXTON G. A. Modeling the effects of vegetation on fluid flow through an acid mine drainage passive remediation system[J]. **Ecological Engineering**, 2018, 110: 27-37.

[35] GUO Z. L., and SHU C. Lattice Boltzmann method and its applications in engineering. **Word Scientific Publishing Cooperation Limited**, Singapore.2013.

[36]HE Y. L., WANG Y. and LI Q. Theory and applications of lattice Boltzmann method. **Beijing Science Press**, Beijing, 2009.

[37]BHATNAGER P. L., GROSS E. P. and KROOK M. A model for collision processes in gases[J]. **Physics Review,** 1954, 94: 511-525.

[38]MOHAMAD A. A. Lattice Boltzmann method-fundamentals and engineering applications with computer codes[M]. **Springer London Dordrecht Heidelberg,** New York, 2011.

[39] QIAN Y. H., D'HUMIERES D. and LALLEMAND P. Lattice BGK models for Navier-Stokes equations [J]. **Europhysics Letters,** 1992, 17, 479-484.

[40] D'HUMIERES D. Generalized lattice Boltzmann equations [J]. **In Rarefied Gas Dynamics: Theory and Simulations,** 1992, 159: 450-458.

[42]LIU C., LIU X. N. and YANG K. J. Predictive model for stage-discharge curve in compound channels with vegetated floodplains [J]. **Applied Mathematics and Mechanics,** 2014,35(12): 1495-1508.

[42] KAZEMI E. NICHOLS A., TAIT S. J., and SHAO S. D. SPH modelling of depth-limited turbulent open channel flows over rough boundaries[J]. **International Journal for Numerical methods in Fluids**, 2017, 83(1): 3-27.

[43] GABREIL E., TAIT S. J. SHAO S,, and NICOLS A. SPHysics simulation of laboratory shallow free surface turbulent flows over a rough bed [J]. **Journal of Hydraulic Research**, 2018, 56(5): 727-747.

[44] SHAO S. D., LO E. Y. M. Incompressible SPH method for simulating Newtonian and non-Newtonian flows with a free surface [J], **Advances in Water Resources,** 2003, 26(7): 787-800.